Journal of Alloys and Compounds 953 (2023) 170020

Contents lists available at ScienceDirect

Journal of Alloys and Compounds

journal homepage: www.elsevier.com/locate/jalcom

A site-selective fluorescence spectroscopy study of the crystal phases of KY_3F_{10}: Leveraging the optical response of Eu^{3+} ions

Pablo Serna-Gallén [a,*], Héctor Beltrán-Mir [a], Eloísa Cordoncillo [a,*], Rolindes Balda [b,c,d], Joaquín Fernández [d]

[a] Departamento de Química Inorgánica y Orgánica, Universitat Jaume I, Av. Vicent Sos Baynat s/n 12071, Castelló de la Plana, Spain
[b] Departamento de Física Aplicada, Escuela de Ingeniería de Bilbao, Universidad del País Vasco UPV-EHU, 48013 Bilbao, Spain
[c] Materials Physics Center CSIC-UPV/EHU, 20018 San Sebastián, Spain
[d] Donostia International Physics Center DIPC, 20018 San Sebastián, Spain

ARTICLE INFO

Article history:
Received 16 February 2023
Received in revised form 24 March 2023
Accepted 6 April 2023
Available online 12 April 2023

Keywords:
Fluoride
Europium
FLN
Luminescence
Crystal Phase

ABSTRACT

The present work deals with the investigation of the site-selective symmetries in Eu^{3+}-doped KY_3F_{10} with different crystal phases. Employing time-resolved fluorescence line-narrowing (TRFLN), a study of the luminescent response of the dopant is reported in samples presenting a single δ-phase, a single α-phase, and a mixture of both δ and α. A new, simple, very low time-consuming and high-yield method was developed to obtain nanospheres of the δ-phase. For both crystal phases, the main site symmetry is spectrally corroborated with that expected by the crystallographic substitution position (C_{2v} in δ, and C_{4v} in α). In addition, the accuracy of the measurements also unveils the presence of significantly distorted Eu^{3+} ions in the surface of the nanoparticles in all the samples studied, a spectral behavior commonly found in glassy systems. All these findings contribute to the proper understanding of the optical response of luminescent dopants in this and related types of complex fluorides. It is worth highlighting the fact that the huge potential of the unexplored δ-phase is demonstrated, since the site-selective emission of the Eu^{3+}-doped δ-phase is up to 20 times more intense than that of the α-phase.

1. Introduction

The present generation of technology calls for innovative approaches and developments which require novel materials with intriguing features. While the goals seem to be straightforward enough, they are subjected to sweeping and complex changes across the scientific community so as to give a response to several demands. On this basis, the last few decades have witnessed a huge growth in the use of fluoride hosts doped with lanthanide ions (Ln^{3+}) for important applications in photonics, biomedicine, and environmental science, to name but a few [1–5]. The implementation of these materials in such fields is based on their outstanding luminescence properties, which arise from the partially filled *f*-orbitals of Ln^{3+} ions, along with the common low phonon energy and the feasibility of being used for (up/down)conversion [6–8].

In recent years, there has been considerable interest in the complex fluoride KY_3F_{10} and its Ln^{3+}-doped counterparts. To date, researchers have been focusing only on the common α-phase of this structure in an attempt to fully describe its physicochemical properties and applications [9–13]. Notwithstanding, in 2000 Le Berre et al. [14] discovered a new crystal phase of this compound, the δ-phase, but it fell into oblivion and no further studies were conducted.

To fill this gap in the literature and explore the potential of this material, we recently developed a new improved method of synthesis using sonochemistry to obtain the δ-KY_3F_{10}·xH_2O compound [15]. This approach yielded truncated triangular nanoplates that were also doped with Eu^{3+} as a first attempt to analyze their luminescent response. Additionally, another complementary study conducted by our laboratory has been published in which the complex formation mechanism of the δ-phase is discussed in detail [16]. The nanoplate-type morphology can be well appropriated for some particular applications, although when it comes to surface engineering and further modifications (such as designing Ln^{3+}-doped core-shell structures), it is of interest to have materials preferably with a spherical morphology. Therefore, efforts in this line have been addressed herein.

From a crystallographic point of view, both α and δ crystal phases exhibit certain similarities: they possess the same crystalline system (cubic), and the spatial groups are very similar. However, the

* Corresponding authors.
E-mail address: pserna@uji.es (P. Serna-Gallén).

https://doi.org/10.1016/j.jallcom.2023.170020

Table 1
Distribution of α-KY_3F_{10} atoms in space group $Fm\bar{3}m$ (no. 225) and δ-$KY_3F_{10}{\cdot}xH_2O$ atoms (labeled with ') in space group $Fd\bar{3}m$ (no. 227).

Name	Species	Wyckoff Position	Local Symmetry	Atomic Coordinates			Occupation Factor
				x	*y*	*z*	
K	K^+	8*c*	T_d (−43m)	1/4	1/4	1/4	1
Y	Y^{3+}	24*e*	C_{4v} (4m.m)	0.2401	0	0	1
F1	F^-	32*f*	C_{3v} (.3m)	0.1081	0.1081	0.1081	1
F2	F^-	48*i*	C_{2v} (m.m2)	1/2	0.1647	0.1647	1
K'	K^+	16*c*	D_{3d} (.−3m)	0	0	0	1
Y'	Y^{3+}	48*f*	C_{2v} (2.mm)	0.4469	1/8	1/8	1
F1'	F^-	96*h*	C_2 (..2)	0	0.3751	0.6249	1
F2'	F^-	32*e*	C_{3v} (.3m)	0.2882	0.2882	0.2882	1
F3'	F^-	32*e*	C_{3v} (.3m)	0.4462	0.4462	0.4462	1
O'	H_2O	48*f*	C_{2v} (2.mm)	0.255	1/8	1/8	0.333

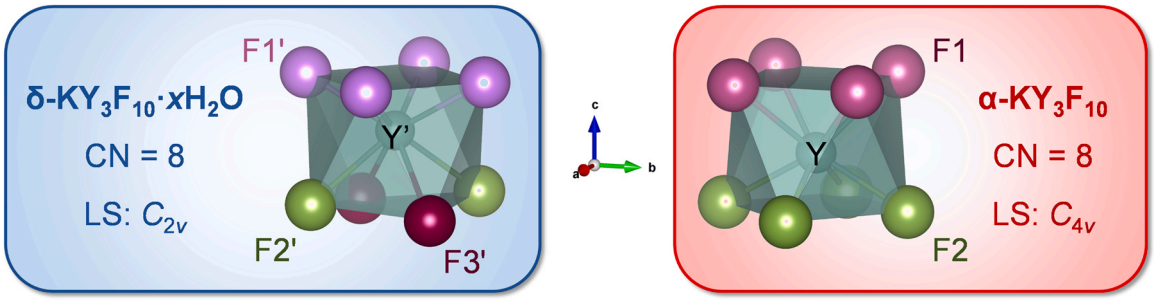

Fig. 1. Coordination polyhedra of Y^{3+} in the different crystal phases of KY_3F_{10}. The corresponding coordination numbers (CN) and local symmetries (LS) are also included.

resulting unit cells and packing have remarkable differences, which can greatly affect the optical performance of the luminescent ions embedded in such hosts. The crystallographic parameters of the different crystal phases of KY_3F_{10} are summarized in Table 1 [17,18], while the coordination polyhedra of Y^{3+} are depicted in Fig. 1 for better understanding. The structures were plotted with VESTA software [19].

On the other hand, it also has to be considered that Le Berre et al. [14] described the isotypic δ-$(H_3O)Y_3F_{10}{\cdot}xH_2O$ crystal phase (containing hydronium ions instead of potassium). Nevertheless, again there is scarce research addressing this compound in the literature [20–24]. The most interesting contribution might be that of Caron et al. [22], which is the only one that has focused on the properties of this compound acting as a host lattice for materials with optical applications. They reported the synthesis and characterization of low-polydispersity, luminescent δ-$(H_3O)Y_3F_{10}{\cdot}xH_2O$ single-crystal nanoparticles doped with Eu^{3+}. Although the particle shape was very controllable (octahedral), the reverse microemulsion method employed required a long time (one week plus purification). Caron's paper suggested the presence of different environments for Eu^{3+}, in the core and on the surface of nanoparticles, characterized by different lifetimes and different emission probabilities. They drew this conclusion considering conventional luminescence studies, but they stated that such an explanation was somewhat speculative and required further sophisticated spectroscopic analysis.

It goes without saying that Eu^{3+} is one of the most appreciated luminescent lanthanide ions due to its particular spectral features and its ability to act as a site-sensitive structural probe [25,26]. Taking this into account, fluorescence line-narrowing (FLN) emerges as the most powerful spectroscopic technique to discriminate among different crystal environments of luminescent ions, which is crucial for understanding their optical performance and the final properties of photonic materials.

FLN is a cryogenic technique used to obtain high-resolution fluorescence spectra [27], which was first applied in solids by Szabo to study a ruby sample [28]. This technique makes it possible to investigate the spectral transitions in solids while at the same time removing the inhomogeneous broadening. In solid-state hosts, FLN has been mainly used to analyze in detail the effects of homogeneous and inhomogeneous broadening in the emission spectra of bulk samples. While homogeneous broadening is associated with the finite linewidth inherent to the emission of "equal" ions (i.e., sensitive to the same crystal field), inhomogeneous broadening is attributed more to the impurities (or dopants) present in a host lattice that cause different Stark effects in the emitter centers (separated energetically in an inhomogeneous way) [29,30]. All this unavoidably entails the difficult interpretation of the emission spectrum of doped compounds in their bulk form. This fact is accentuated in glasses, where a greater component of disorder and thus inhomogeneous broadening, might be expected [31,32]. However, due to the *finesse* of the FLN technique, this problem can be easily overcome and it is easy to selectively discriminate among different crystal-field environments for a given dopant ion in complex systems, such as those presenting a mixture of crystal phases, as will be outlined in the present work.

FLN experiments are sensitive to local sites of the dopant ion in the host lattice because laser-selected energy levels are associated with specific single sites of distinct symmetry [33]. Hence, if the linewidth of the excitation laser is narrower than the inhomogeneously broadened line width of a sample, only part of the ions of narrow spectral definition are excited [34]. For the particular case of Eu^{3+}, the laser frequency is tuned over the inhomogeneous bandwidth of the $^7F_0$–$^5D_0$ transition. Since no Stark splitting can occur in the $^5D_0$ state under any symmetry and the $^7F_0$ state is also non-degenerate, the spectral profile due to $^5D_0 \rightarrow {}^7F_J$ emissions is only determined by the splitting of the terminal levels caused by the local crystal field of Eu^{3+} ions at different sites [35–37].

Bearing in mind everything mentioned above, in this paper a full study of the Eu^{3+} ions embedded in both α and δ crystal phases of KY_3F_{10} is reported employing FLN spectroscopy. Furthermore, a new, simple, very low time-consuming and high-yield method is presented to obtain nanospheres of the δ phase, which allows comparison of the optical response of the different phases. Our findings are vital to understand the optical response of Eu^{3+} and other

dopants in these types of fluorides thanks to the description of the sites occupied by the rare earth. The results underscore the huge potential of the unknown δ-phase, since the site-selective emission of the Eu^{3+}-doped δ-phase is up to 20 times more intense than that of the α-phase.

2. Experimental section

2.1. Materials

The reagents used for the synthesis of the materials were yttrium (III) nitrate hexahydrate [$Y(NO_3)_3{\cdot}6H_2O$ 99.8 %], europium(III) nitrate hexahydrate [$Eu(NO_3)_3{\cdot}6H_2O$ 99.9 %], potassium fluoride [KF 99.5 %], potassium tetrafluoroborate [KBF_4 96 %], and hydrofluoric acid aqueous solution [HF 40 % wt.]. All reagents were purchased from Sigma-Aldrich, except europium(III) nitrate hexahydrate (Strem Chemicals), and used without further purification.

2.2. Synthesis and characterization of materials

For all the syntheses described below, calculations were performed to obtain approximately 0.25 g of the α/δ-phase(s) of $KY_3F_{10}{\cdot}xH_2O$. Different amounts of the luminescent Eu^{3+} ion were employed in the three series of samples: KLn_3F_{10} (Ln = Y, Eu; 1, 3, 5 mol% Eu^{3+}). A summary of the abbreviations used according to the dopant content and the crystal phases(s) obtained is indicated in Table 2. The general scheme of the three synthetic routes is depicted in Fig. 2.

2.2.1. Preparation of δ-KY_3F_{10}:Eu^{3+}

A new, fast, and easy coprecipitation method was developed to prepare the δ-phase compounds. First, 1.5 mmol of $Ln(NO_3)_3{\cdot}6H_2O$ were dissolved in 10 mL of water. Then, another solution was prepared by dissolving 3 mmol of KF in 10 mL of water and, subsequently, adding 135 µL of HF aqueous solution 40 wt% (3 mmol). Later, the KF/HF solution was added dropwise to the previously prepared Ln^{3+} solution. While doing so, a white precipitate appeared and the mixture was kept under vigorous stirring for 1 h at room temperature. After that, the precipitate was collected by centrifuging the mixture and washing it twice with water. Finally, it was dried under an infrared lamp. It is worthwhile noting that the original synthetic method proposed by Le Berre et al. [14] in 2000 (when this material was discovered) required the use of ≈ 20 mL of HF 40 wt% for the synthesis of similar amounts of powder. Thus, this new experimental procedure greatly reduces the use of hydrofluoric acid, which is well known for its harmful effects on human health.

2.2.2. Preparation of (δ + α)-KY_3F_{10}:Eu^{3+}

The powders were prepared following the same protocol as for the synthesis of the δ-phase compounds. Notwithstanding, it is important to highlight that instead of adding the KF/HF solution dropwise, a fast addition was required to obtain a mixture of the two crystal phases.

2.2.3. Preparation of α-KY_3F_{10}:Eu^{3+}

Eu^{3+}-doped fluorides with α-phase were obtained following a sonochemical process based on some previous studies of our research group described in references [16,38]. For that purpose, the fluoride source employed was KBF_4. The final solution was transferred into a *Bandelin Sonorex* ultrasonic bath operating with a frequency of 35 kHz for 6 h at room temperature.

Table 2
Nomenclature of the KY_3F_{10} fluorides prepared at different mol% Eu^{3+}.

% Eu^{3+}	Crystal Phase		
	δ	δ + α	α
1	1D	1DA	1A
3	3D	3DA	3A
5	5D	5DA	5A

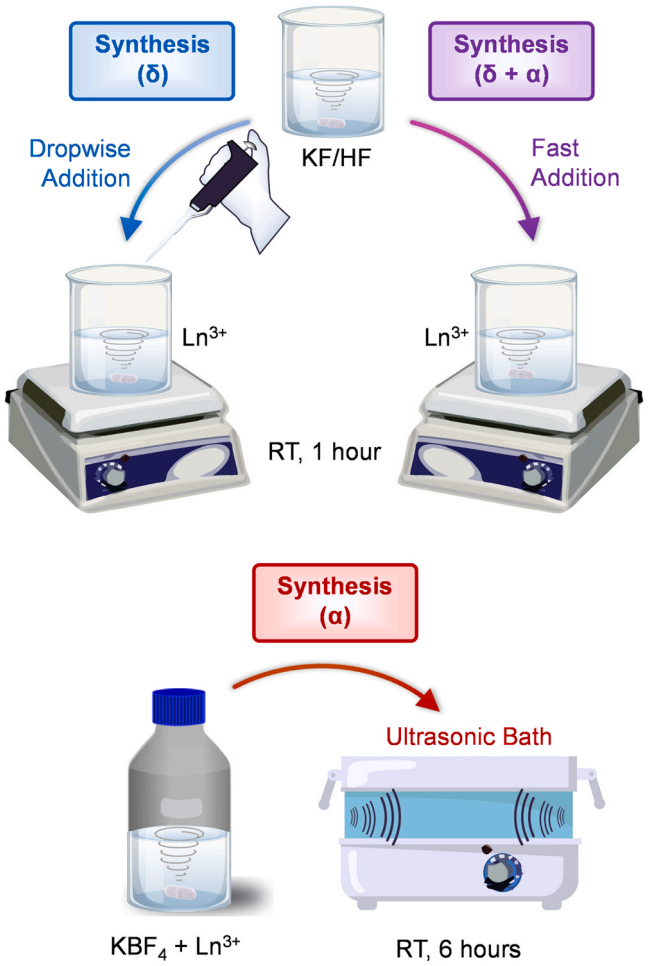

Fig. 2. General scheme for the preparation of samples with different crystal phases of KY_3F_{10}.

2.3. Characterization

Powder X-ray diffraction (XRD) was performed at room temperature using a Bruker-AX D8-Advance X-ray diffractometer with $CuK_{\alpha 1}$ radiation from 2θ = 15–90° at a scan speed of 1.8°/min. The FT-IR spectra of the solids were recorded using an Agilent Cary 630 FT-IR spectrometer in transmission mode. Thermal analysis was carried out by a simultaneous thermogravimetric analysis (TG) and differential scanning calorimetry (DSC) using Mettler Toledo TGA/DSC3 equipment (Al_2O_3 crucible, argon atmosphere, 5 °C/min heating rate, 25–550 °C).

Besides, the microstructure of samples was observed using a JEOL 7001F scanning electron microscope (SEM) operating with an acceleration voltage of 30 kV. For microstructural characterization, the powders were deposited on carbon double-sided stickers (previously adhered to the surface of aluminum stubs) and were sputtered with platinum. Dynamic Light Scattering (DLS) size distribution measurements were recorded using a Zetasizer Nano-ZS90 (Malvern Instruments, UK). Automatic optimization of beam focusing and attenuation was employed for each sample.

Resonant time-resolved fluorescence line-narrowing (TRFLN) spectra were performed by exciting the samples with a pulsed

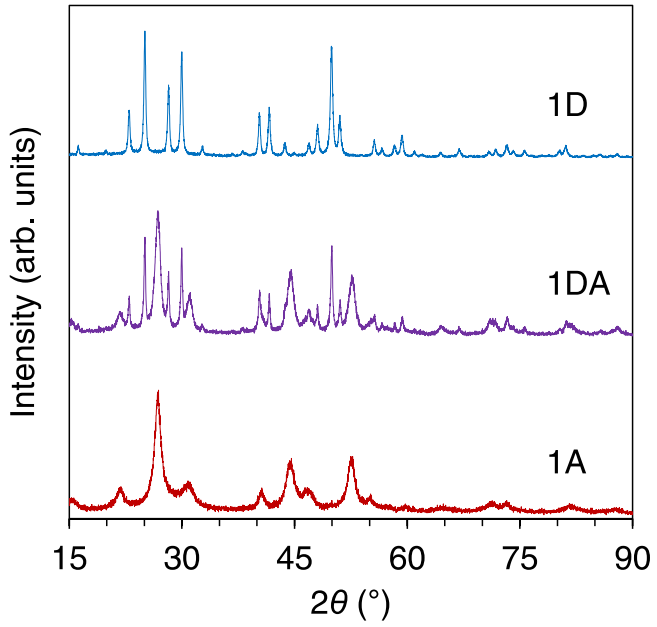

Fig. 3. XRD patterns of samples doped with 1 mol% Eu^{3+} content.

frequency doubled Nd:YAG pumped tunable dye laser with a 9 ns pulse width and 0.08 cm^{-1} line width, and detected by an EGG&PAR Optical Multichannel Analyzer. The measurements were carried out at 9 K in a closed cycle helium cryostat.

3. Results and discussion

3.1. Structural and thermal characterization

The XRD patterns of the Eu^{3+}-doped samples (1 mol% Eu^{3+}: 1D, 1DA, 1A) prepared using the different synthetic routes are presented in Fig. 3 as representatives of each series of samples. For higher percentages of dopant (3 and 5 mol% Eu^{3+}), the same XRD profiles were obtained. Sample 1D exhibits the peaks corresponding to a single phase of cubic δ-KY_3F_{10}·xH_2O (ICDD card 04–016–7073). Nonetheless, the speed of the addition of the fluoride source (KF/HF solution) into the Ln^{3+} solution has a profound influence on the resulting crystal phase formation. A fast addition leads the system towards the formation of α-KY_3F_{10} in coexistence with the δ-phase (sample 1DA). For a better interpretation of these results, the peaks of the α-KY_3F_{10} structure (ICSD card 00-040-9643) can be well appreciated in the XRD pattern of sample 1 A. This result underscores how delicate this fluoride system is. Further complementary and computational work, which will be the topic of an upcoming publication, is under study and corroborates that the α phase is slightly more thermodynamically favorable than the δ phase, which would explain the delicate equilibrium of coexistence between the two structures.

As outlined, the presence of both crystal phases in the same sample is a matter of study. Hence, to go deeper into this and have a semi-quantitative value of the corresponding phase fractions in the sample, the XRD pattern of sample 1DA was refined using the Rietveld method. Further details can be found in Section S1 of the Supporting Information. The results revealed that sample 1DA is composed of, approximately, 69 % of α-phase and 31 % of δ-phase.

In order to complement the structural characterization of the materials, FT-IR spectra of samples doped with 1 mol% Eu^{3+} content (i.e., 1D, 1DA, 1 A) were recorded and are presented in Fig. S2 of the Supporting Information. The spectra showed the characteristic bands associated with the corresponding internal vibrations, and exhibited changes in the position and amplitude of the peaks depending on the different crystal phase(s). For the three compositions, the presence of absorbed/crystalline water was also noted.

To study the thermal behavior of the powders and also corroborate the existence of single/multiple crystal phase(s), simultaneous thermogravimetric analysis (TG) and differential scanning calorimetry (DSC) experiments were conducted for all the samples. The TG/DSC curves are depicted in Fig. 4, while the weight loss percentages and x values for KLn_3F_{10}·xH_2O (Ln = Y, Eu) compositions are summarized in Table 3. Each series of samples (i.e., compounds with δ, δ + α, and α crystal phases doped at different concentrations of Eu^{3+}) exhibited virtually the same thermal behavior. Powders with a δ-KY_3F_{10}·xH_2O structure (1D, 3D, 5D) presented a progressive loss of mass associated with the crystalline water inside the channels and cavities of the crystal structure as well as with some absorbed water. According to these data, the number of water molecules in these compositions was established to be $x \approx 2.8$ (see Table 3). In addition, the absence of multiple/notable (endo/exo)thermic peaks in the temperature range 25–300 °C underscores the fact that there are no apparent traces of a possible δ-$(H_3O)Y_3F_{10}$·xH_2O phase. The exothermic peak found at 418 °C is associated with the topotactic δ→α phase transition [14], which is in agreement with the above-mentioned stability of the α phase and the delicate equilibrium of possible coexistence between the two structures.

On the other hand, compounds with the α-KY_3F_{10} structure (1A, 3A, 5A) also presented a progressive loss of mass, although associated only with absorbed water rather than crystalline water, since this phase does not present any zeolitic cavities that allow the incorporation of crystalline water molecules inside the structure. This result is also corroborated by the lower percentage of weight loss in comparison to samples with the α-phase. Indeed, the number of water molecules in these compositions was established to be $x \approx 1.7$ (see Table 3). Besides, the TG/DSC results for samples with the coexistence of both crystal phases (1DA, 3DA, 5DA) are in direct connection with the FT-IR spectra (see Supporting Information for further details). The thermal behavior of these three compositions can be explained by considering an intermediate response between samples exhibiting a single δ- and α-phase. It is worthwhile pointing out that the weight loss percentage and the number of water molecules ($x \approx 1.7$) are essentially the same as for samples with a single α-phase, which is in very good agreement with the results obtained from the Rietveld refinement that underline the prevalence of the α-phase. Therefore, this result confirms that there is a higher amount of this crystal phase, which is also in agreement with the position and amplitude of the FT-IR bands. Nonetheless, the presence of particles with a δ-phase can be well inferred from the DSC curve since the exothermic peak associated with the topotactic δ→α phase transition is also present, although with a smaller area and appearing at lower temperatures.

3.2. Morphological characterization

The morphologies of the as-prepared products are illustrated in Fig. 5**.** The SEM images correspond to samples 1D (δ), 1DA (δ + α), and 1 A (α) as representatives of the different crystal phases. There were no appreciable morphological/size changes while increasing the dopant content in each series of samples. Powders with δ-phase exhibited a homogeneous distribution of spherical nanoparticles (between 160 and 190 nm). Interestingly, the higher magnification SEM image demonstrated the presence of self-assembled nanospheres around 40 nm in diameter, Fig. 5(a). Simultaneously, it is noteworthy that the new synthetic procedure herein described to prepare δ-KY_3F_{10}·xH_2O compounds yields spherical particles, which can be of great interest for the development of core-shell type structures or further surface modifications/coatings. The previous method of synthesis developed by our laboratory to generate

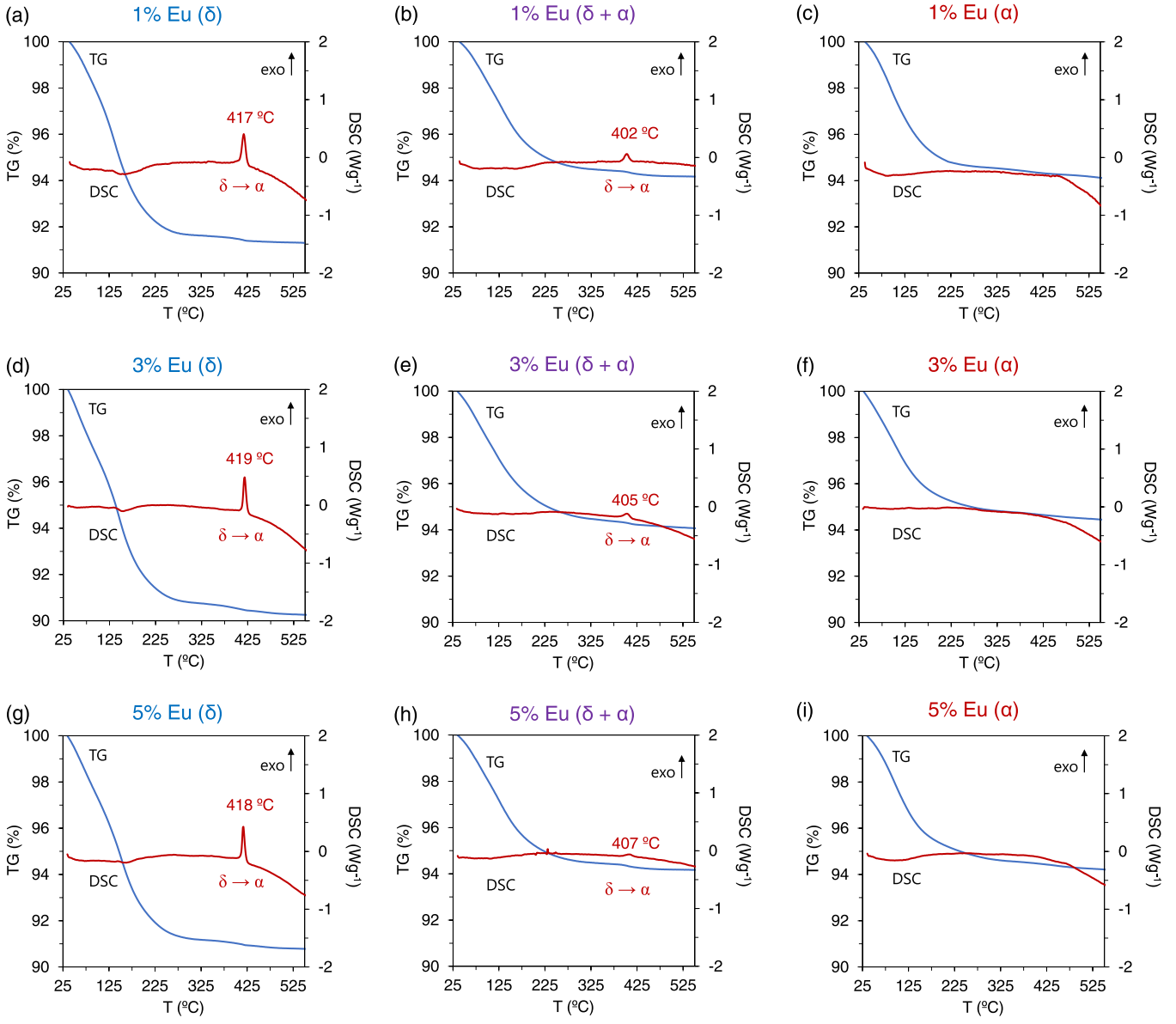

Fig. 4. TG/DSC curves for samples 1D (a), 1DA (b), 1A (c); 3D (d), 3DA (e), 3A (f); 5D (g), 5DA (h), and 5A (i).

Table 3
Weight loss percentages and *x* values for $KLn_3F_{10}{\cdot}xH_2O$ (Ln = Y, Eu) compounds with 1 mol% Eu^{3+} content.

Sample	Weight loss (%)	*x*
1D	8.7	2.6
3D	9.7	3.0
5D	9.2	2.8
1DA	5.8	1.7
3DA	5.9	1.7
5DA	5.7	1.7
1A	5.9	1.7
3A	5.5	1.6
5A	5.8	1.7

fluorides with this structure produced truncated triangular nanoplates that also formed aggregates in order to reduce the surface energy [15], which are drawbacks that could prevent the possibility of making well-controlled and good surface engineering.

Regarding the compositions with a mixture of crystal phases – sample 1DA in Fig. 5(b) – a significant change in the morphology was appreciated. The powder consists mainly of an amorphous-type matrix (highlighted in red) in which some nanospheres (highlighted in blue) are embedded. The major presence of the heterogeneous part is consistent with the previous XRD, FT-IR, and TG/DSC results since this predominant morphology might be well ascribed to the α-phase, while the nanospheres (some colored in blue as an example) correspond to the δ-phase particles. At first glance, this fact can be well corroborated by comparing Fig. 5(a) and (b). The reason for the formation of the heterogeneous matrix is mainly due to the speed of the addition of the fluoride source (KF/HF solution) into the Ln^{3+} solution. For the latter case, a rapid addition was performed to produce the powders, while the dropwise addition used in the formation of δ-$KY_3F_{10}{\cdot}xH_2O$ compounds explains the homogeneous and well-distributed nature of the nanospheres.

Finally, Fig. 5(c) shows a typical SEM image of sample 1A (α-phase), which was prepared by an ultrasonication process. This sample consists of spherical particles (most of them around 400 nm) which resulted from the self-assembly of nano-sized subunits around 10–20 nm in diameter.

Furthermore, in order to get a better idea of the particle size distribution, Dynamic Light Scattering (DLS) size distribution

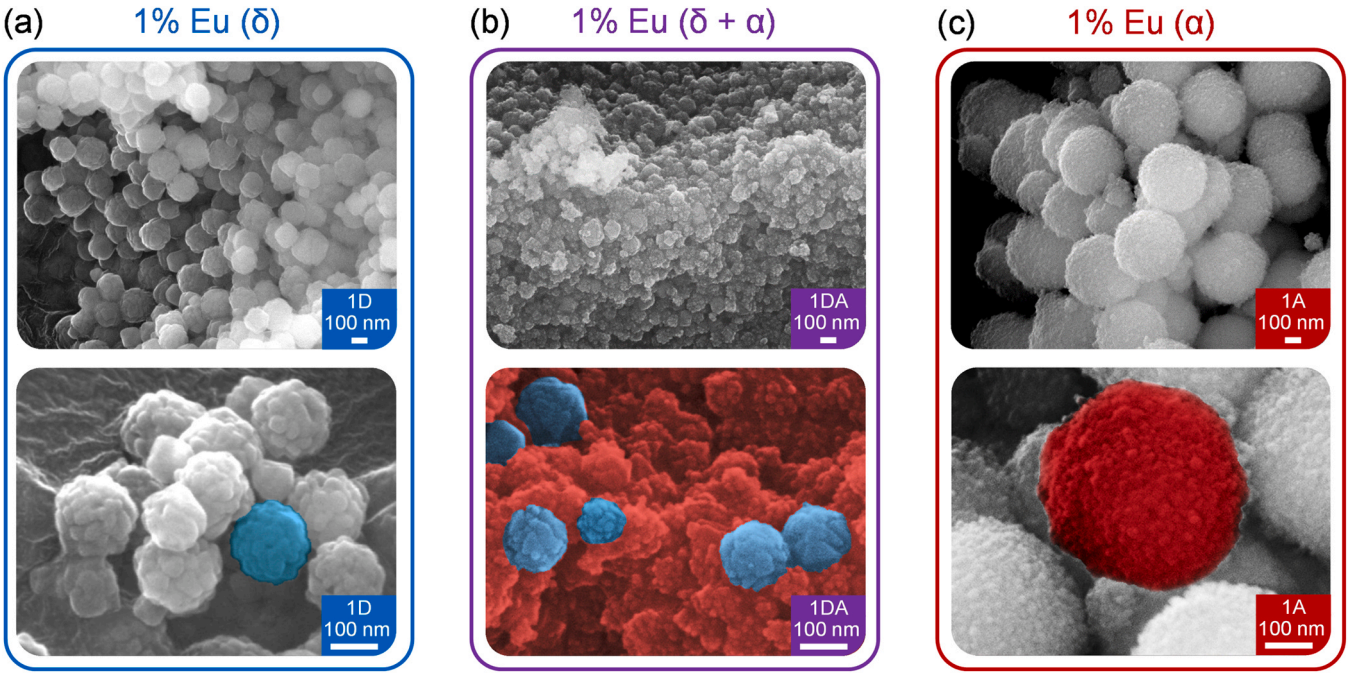

Fig. 5. SEM images for samples 1D (a), 1DA (b), and 1 A (c).

measurements were recorded. The hydrodynamic diameters obtained were in very good agreement with the SEM results, Fig. S3 of the Supporting Information.

3.3. Photoluminescence studies

3.3.1. Site-selective time-resolved fluorescence line-narrowing spectroscopy

i) *General grounds*

The electronic energy levels of an isolated impurity in a solid are very sensitive to the positions of the nearby atoms. Since the frequency of a particular electronic transition of the impurity is directly proportional to the difference between the energies of the relevant pair of levels, it is clear that precise optical spectroscopy of the impurity can provide information about the positions and distribution symmetry of the impurity surrounding atoms in the host solid. However, the problem is far from simple. On the one hand, the electronic wave functions and the distances between the electronic levels of the chromophore depend on their environment and, on the other, in general, the electronic transitions also modify the distribution of vibrational states in the solid, which in turn can have an influence on electronic transitions. The case we are interested in concerns a substitutional rare-earth (RE) ion, used as a spectral probe, which interacts only weakly with its rigid host, so we expect the local environment to affect only the electronic energy and not the normal mode vibrational frequencies. Thus, in the discussion that follows, we will only consider a single broadened vibrational line shape for all vibrational lines associated with a given electronic transition

Our aim is to identify the possible crystal field (CF) symmetry distortions felt by the RE paramagnetic impurity embedded in the crystal lattice sites of the different phases of this fluoride nanocrystal, as well as to analyze the influence of the lattice distortions near the nanoparticle surface on the RE emission. Among trivalent lanthanide ions, Eu^{3+} is particularly attractive as a CF probe because of the relatively simple Stark structure of the ^7F_J and the ^5D_J states for $J = 0, 1, 2$. Moreover, excitation of Eu^{3+} fluorescence is possible at a low temperature between $^7F_0$ and $^5D_0$ singlet states. For this purpose, we have used a laser-induced site-selective time-resolved fluorescence line-narrowing technique (TRFLN). A tunable pulsed (9 ns pulse width) dye laser (0.08 cm^{-1} line width) was used as the excitation source and an optical multichannel analyzer with a gated intensified CCD detector to collect the time-resolved resonant and non-resonant $^5D_0 \rightarrow {}^7F_J$ emissions.

ii) *Interpretation of the TRFLN spectra*

Although the fundamentals of the fluorescence line-narrowing (FLN) technique may seem simple, it is advisable to have a clear idea, from the theoretical point of view, about what interpretative complications may arise. Therefore, we are going to briefly comment on some basic aspects of the model that describes the absorption/emission processes. The aim is to use intense monochromatic laser irradiation to excite a subset of Eu^{3+} ions with nearly identical crystal strain shifts within a possible inhomogeneously broadened absorption profile. If the impurity centers exist in a distribution of environments, these spectra will be shifted with respect to each other because the crystal host fields primarily affect the electronic transition energy. If the central electronic transition frequency for a given center is ν_0, we can express the absorption spectrum summed for all the Eu^{3+} centers in the ensemble as

$$S(\nu) = \int D(\nu_0) A(\nu - \nu_0) d\nu_0 \quad (1)$$

where $A(\nu - \nu_0)$ is the intrinsic absorption spectrum shape of a center at the electronic transition frequency ν_0 and $D(\nu_0)$ is the distribution function that gives the probability that a center will have electronic transition energy ν_0. If the sample is irradiated with a laser whose output spectrum is $\mathscr{L}(\nu - \nu_L)$, then the distribution of excited centers is given by

$$P(\nu_0) = D(\nu_0) A(\nu - \nu_0) \mathscr{L}(\nu - \nu_L) \quad (2)$$

and if the emission spectrum of the europium center with an electronic transition frequency ν_0 is given by $\mathscr{E}(\nu' - \nu_0)$, then the emission spectrum of the laser-irradiated fluoride crystal powder will be given by

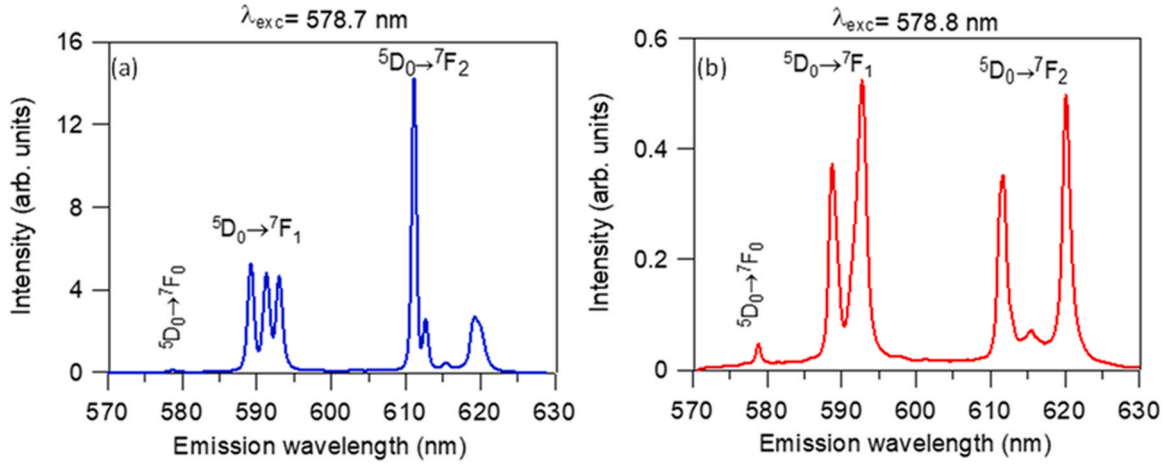

Fig. 6. Low temperature (9 K) TRFLN emission spectra of the $^5D_0 \rightarrow {}^7F_{0,1,2}$ transitions for the samples (a) 1D, Eu^{3+} 1 %-δ, and (b) 1 A, Eu^{3+} 1 %-α, obtained under excitation at 578.7 nm and 578.8 nm respectively in the $^7F_0 \rightarrow {}^5D_0$ transition.

$$S(\nu') \propto \iint D(\nu_0) A(\nu - \nu_0) \mathcal{L}(\nu - \nu_L) \mathcal{E}(\nu' - \nu_0) d\nu_0 d\nu \tag{3}$$

If the laser line width is very narrow, as compared to the inhomogeneously broadened absorption, the laser spectrum can be substituted by a delta function at ν_L and the above expression becomes

$$S(\nu') \propto \int D(\nu_0) A(\nu_L - \nu_0) \mathcal{E}(\nu' - \nu_0) d\nu_0 \tag{4}$$

Thus, the output spectrum is expressed as a convolution of both absorption and emission of a given distribution $D(\nu_0)$ of Eu^{3+} centers.

It can be assumed that in the low-temperature limit the line shape for both absorption and emission of a single Eu^{3+} center, with a very narrow strain distortion and interaction with a single phonon mode, can be described as the sum of a narrow zero-phonon line (Z) and a broad phonon wing (W) contribution weighted by a temperature-dependent Debye-Waller factor (F) [39,40].

$$S_{abs}(\nu - \nu_0) = (F) Z_{abs}(\nu - \nu_0) + (1 - F) W_{abs}(\nu - \nu_0) \tag{5}$$

$$S_{em}(\nu_0 - \nu) = (F) Z_{em}(\nu_0 - \nu) + (1 - F) W_{em}(\nu_0 - \nu) \tag{6}$$

When Eu^{3+} ions are pumped by spectrally narrow laser light of frequency ν_L, the distribution of the excited state centers is then given by

$$P(\nu_0) = D(\nu_0)\{F Z_{abs}(\nu_L - \nu_0) + (1 - F) W_{abs}(\nu_L - \nu_0)\} \tag{7}$$

Thus, in general, for a given $D(\nu_0)$ site distribution and temperature, by using expressions (4–7), we would have the output spectrum given by the sum of four contributions:

$$\begin{aligned} S(\nu) &= \int S_{em}(\nu_0 - \nu) P(\nu_0) d\nu_0 \\ &= F^2 \int D(\nu_0) Z_{abs}(\nu_L - \nu_0) Z_{em}(\nu_0 - \nu) d\nu_0 \\ &+ F[1 - F] \int D(\nu_0) Z_{abs}(\nu_L - \nu_0) W_{em}(\nu_0 - \nu) d\nu_0 \\ &+ F[1 - F] \int D(\nu_0) W_{abs}(\nu_L - \nu_0) Z_{em}(\nu_0 - \nu) d\nu_0 \\ &+ [1 - F]^2 \int D(\nu_0) W_{abs}(\nu_L - \nu_0) W_{em}(\nu_0 - \nu) d\nu_0 \end{aligned} \tag{8}$$

The first term corresponds to zero-phonon absorption followed by zero-phonon emission, the second refers to zero-phonon absorption followed by phonon wing emission, the third one gives the zero-phonon emission obtained under wing absorption and, finally, the fourth term gives the phonon wind emission corresponding to phonon wind absorption. In our Eu-fluoride system, electron-phonon coupling seems to be weak because no phonon side band is observed under site-selective excitation at the $^5D_0$ level at low temperature. In addition, there is no evidence of spectral diffusion within the inhomogeneously broadened spectral profile, and so in the following discussion about the TRFLN experimental results, we will only pay attention to the first and third terms in (8), which account for experimentally found narrowed electronic emissions of the Eu^{3+} centers in the fluoride nanocrystals.

iii) *Experimental results and discussion*

Fig. 6(a) shows the $^5D_0 \rightarrow {}^7F_{0,1,2}$ emission spectrum of sample 1D (1 mol% Eu^{3+}-doped δ-phase of KY_3F_{10}) obtained at 10 μs after a 578.7 nm pump pulse corresponding to the $^7F_0 \rightarrow {}^5D_0$ transition. The most intense emission comes from the first component of the $^5D_0 \rightarrow {}^7F_2$ emission containing at least four components. The spectral features still remain if the laser wavelength is tuned a few angstroms at both sides of the $^7F_0 \rightarrow {}^5D_0$ transition but the intensity drops very quickly. The magnetic dipole and allowed $^5D_0 \rightarrow {}^7F_1$ emission is much less intense, showing three spectral components that could correspond to a site with point symmetry C_{2v}, the one found by XRD for the Y^{3+} ion in this phase. On the other hand, the resonant $^5D_0 \rightarrow {}^7F_0$ emission is barely visible. No changes in the shape of the spectral components are observed by changing the delay time at which the detector starts measuring (0–13 ms). All the experiments were performed at 9 K.

Fig. 6(b) displays the $^5D_0 \rightarrow {}^7F_{0,1,2}$ emission spectrum of sample 1 A (1 mol% Eu^{3+}-doped α-phase of KY_3F_{10}) obtained under resonant $^7F_0 \rightarrow {}^5D_0$ excitation with a 578.8 nm pulse. The intensity of the emission is more than an order of magnitude less than in the δ phase. Moreover, the intensities of both $^5D_0 \rightarrow {}^7F_1$ and $^5D_0 \rightarrow {}^7F_2$ transitions are similar. However, in this case, the $^5D_0 \rightarrow {}^7F_1$ emission presents only two spectral components pointing to a higher site symmetry for the europium ion. In fact, this point symmetry would correspond to the C_{4v} point group [41,42] that has been found for Y^{3+} ions by XRD in the α-phase. As can be observed in these figures, from an energetic point of view, the emission efficiency of the δ phase is much higher (> 20 times) than the α one for all the spectral components. This behavior may be related to an increase in the radiative probability associated with the site symmetry distortion of the fluorine ligand crystal field in the δ-phase.

The above low-temperature TRFLN results identify the energy of the $^5D_0$ singlet state of the Eu^{3+} in both phases in the main crystal site occupied by the rare earth (Y^{3+} site) as well as its narrowed emissions from the excited $^5D_0$ level. However, given the size of the crystalline nanoparticles, we expect a significant number of Eu^{3+} ions to lie at sites near the surface, where distortions of the crystal lattice can produce variable crystal fields at europium sites similar to

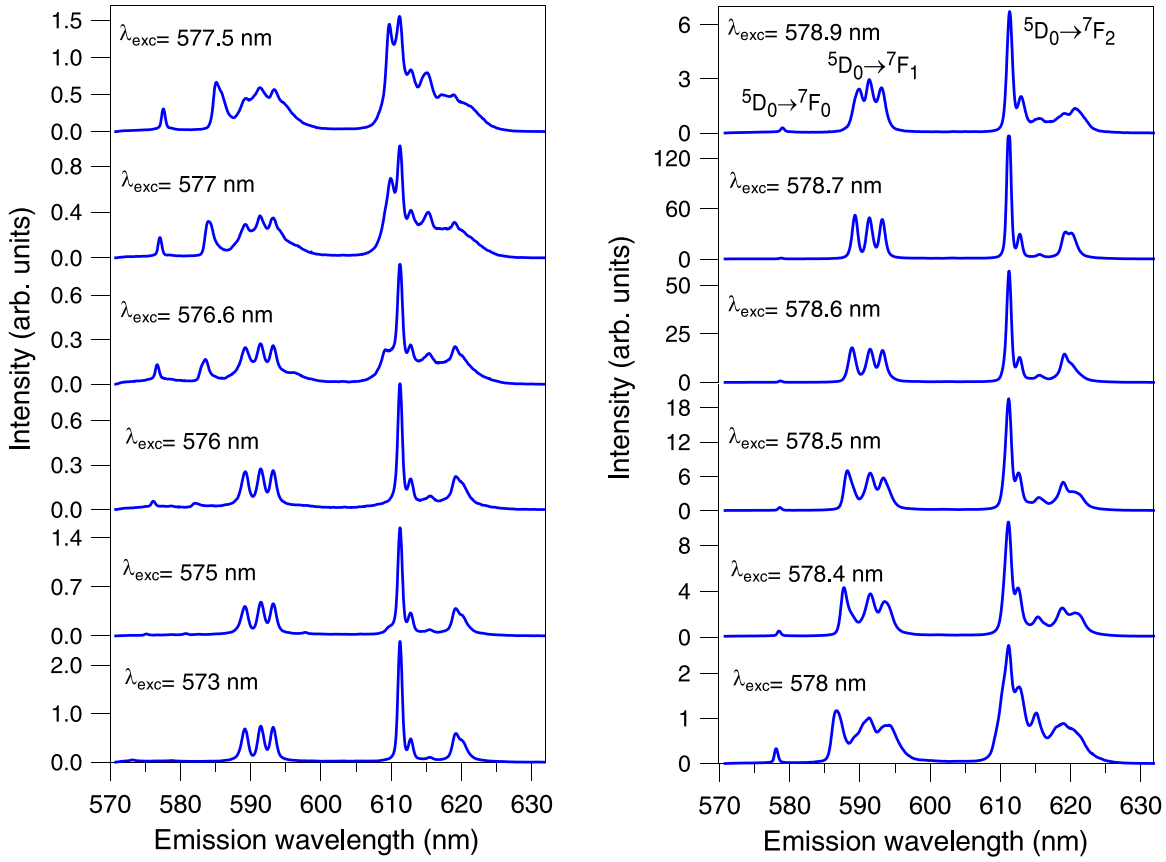

Fig. 7. Low temperature (9 K) TRFLN emission spectra of the $^5D_0 \rightarrow {}^7F_{0,1,2}$ transitions for sample 3D (Eu^{3+} 3 %-δ) obtained at different excitation wavelengths along the $^7F_0 \rightarrow {}^5D_0$ transition.

those produced in a messy medium, like a glass. To investigate this issue, the laser tuning feature of our TRFLN spectroscopy was used. Although the previous experiments conducted to identify the main crystal site of Eu^{3+} were obtained with 1 mol% Eu-doped samples, no significant spectral changes were observed for both lower and higher concentrations of rare earth. Therefore, in order to increase our spectral resolution, given the expected smaller TRFLN signals, in the following experiments we have used 3 mol% Eu^{3+} doped samples for both the α and δ phases.

Taking into account the theoretical predictions of expression (8) for the output spectrum of FLN spectroscopy in the presence of a given $D(\nu_0)$ distribution of chromophore sites in a crystalline matrix, we have performed additional experiments scanning the laser wavelength over a wide range of energies both above and below that corresponding to the main crystal field site found in both phases. The results are displayed in Figs. 7–9 for δ, α, and (δ + α) phases, respectively.

δ phase: Fig. 7 displays a set of twelve selected spectra in the range 570–630 nm corresponding to the resonant and non-resonant emissions $^5D_0 \rightarrow {}^7F_{0,1,2}$. It is worth mentioning that the vertical scale gives the relative intensity of the measured spectra. As the pumping energy increases above the maximum of the $^7F_0 \rightarrow {}^5D_0$ electronic transition of the main Eu^{3+} site (λ_{ex} = 578.7 nm), the Eu^{3+} emission falls 85 % in two angstroms, then both $^5D_0 \rightarrow {}^7F_{1,2}$ emissions broaden and their profiles (see λ_{ex} = 578.0 nm spectrum) are similar to those found by some authors in Eu-doped fluorophosphate glass [43]. This behavior indicates the presence of a quasi-continuous distribution of crystalline fields associated with europium ions in environments where the crystalline lattice is distorted by the presence of surface or subsurface defects that can produce variations in coordination and/or lengths and orientation of the bonds with the rare earth. If we continue exciting at higher energies (see λ_{ex} = 577.5–576.6 nm spectral range), the spectrum widens even more and in the $^5D_0 \rightarrow {}^7F_1$ emission profile more than the three predictable spectral components of a low symmetry site appear. By increasing the excitation energy a little more, we see, with apparent surprise, that the spectral structure of the main europium crystal site reappears and the emission energy slightly increases. The explanation for this is given by the third term of expression (8) mentioned above. Now the narrowed emission from $^5D_0$ is produced by absorption to a vibronic state in the phonon wind. In this case, the electron-phonon process consists of an electronic transition to the $^5D_0$ level of the Eu^{3+} occupying the main site, assisted by the emission of a low-energy phonon to the crystal lattice. As a two-body process, the probability of this kind of process is smaller than that of a direct electron transition, as the measured intensity shows. Furthermore, although we have excited in the phonon sideband, the spectral response is the one that corresponds to the only site present in the bulk crystalline structure. If this were not the case, we could have had a spectral broadening associated with the distribution of the different crystal sites.

α phase: presents a similar spectral behavior but with some differences in the spectral width and shape of the spectra. Fig. 8 displays a sample of the spectra obtained by scanning the laser wavelength in the range 579–573 nm. If we decrease the excitation wavelength by more than two angstroms below that of the main Eu^{3+} site (λ_{ex} = 578.8 nm), the shape of the spectrum widens and begins to change, clearly showing a reduction in point symmetry (C_{2v} or less). An additional component appears in the $^5D_0 \rightarrow {}^7F_1$ transition, and the $^5D_0 \rightarrow {}^7F_2$ components take on a glass-like appearance (see λ_{ex} = 577.7–576.6 nm spectral range). Then, around λ_{ex} = 575 nm, the spectral profile of the tetragonal main site of Eu^{3+} in this crystalline

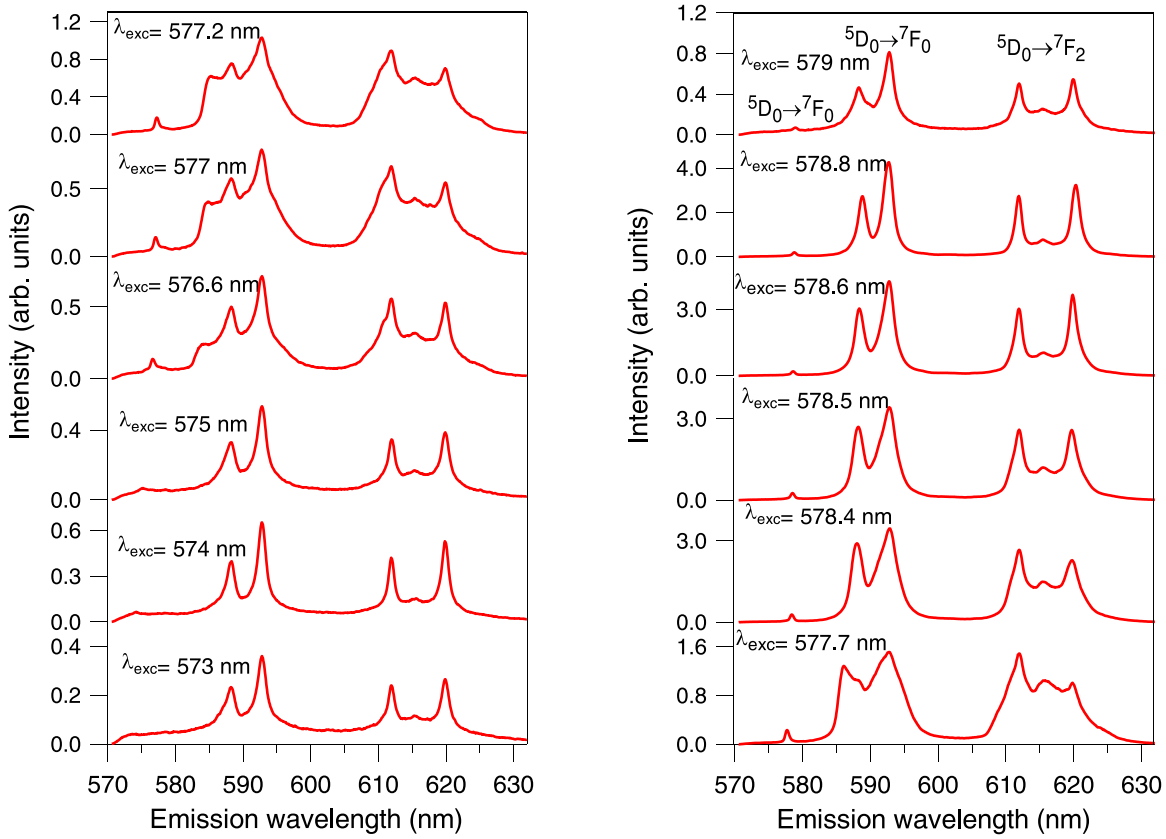

Fig. 8. Low temperature (9 K) TRFLN emission spectra of the $^5D_0 \rightarrow {}^7F_{0,1,2}$ transitions for sample 3 A (Eu^{3+} 3 %-α) obtained at different excitation wavelengths along the $^7F_0 \rightarrow {}^5D_0$ transition.

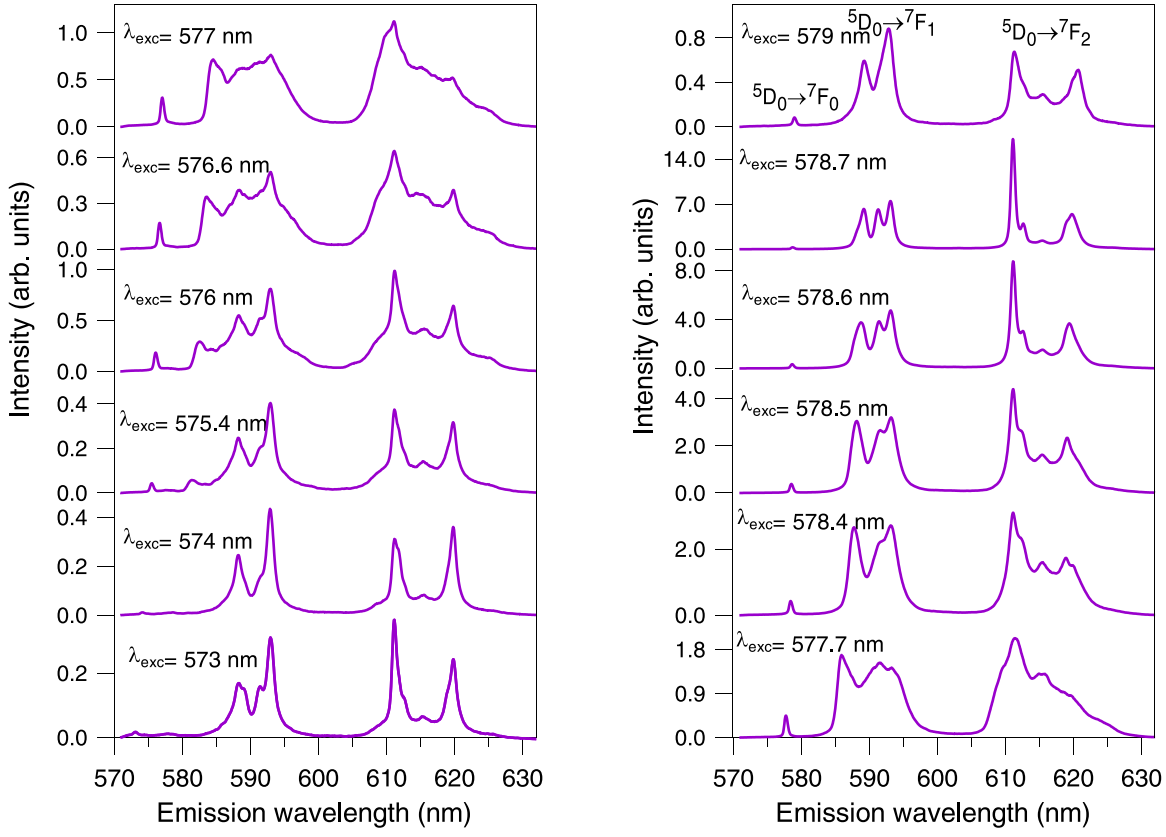

Fig. 9. Low temperature (9 K) TRFLN emission spectra of the $^5D_0 \rightarrow {}^7F_{0,1,2}$ transitions for sample 3DA (Eu^{3+} 3 %-δ + α) obtained at different excitation wavelengths along the $^7F_0 \rightarrow {}^5D_0$ transition.

phase reappears again, helped, as in the δ phase, by the vibronic sideband.

(δ + α) phases: Fig. 9 shows the spectral results for the 3DA (3 mol %-Eu^{3+} doped phase) mixed sample. As we can see, the best spectral resolution for both α and δ phases is obtained by exciting at 579.0 and 578.7 nm respectively. However, the efficiency of the δ phase drops when compared to the sample with only the δ phase. If we compare the relative intensity of the Eu^{3+} emission in α and δ single phase samples with that of the (δ + α) sample, we come to the conclusion that in the sample with both (δ + α) phases the amount of α phase is around twice that of δ. This hypothesis is further confirmed by the emission spectrum obtained by exciting at the high energy vibronic side λ_{ex} = 574 nm. We can see that the only crystal site present is the one corresponding to the α phase. For intermediate excitation wavelengths, the ordinary glass-like behavior with higher influence of the α phase is found (see λ_{ex} = 578.5–575.4 nm spectral range). This result is also in perfect agreement with the phase fraction estimation obtained by the Rietveld refinement.

The lifetimes of the $^5D_0$ level of Eu^{3+} should reflect the different site symmetry for Eu^{3+} ions in the different phases. The experimental decays of the $^5D_0$ level were obtained for all samples at room temperature by exciting at 392.5 nm in the $^7F_0 \rightarrow {}^5L_6$ transition and collecting the luminescence at 612 nm ($^5D_0 \rightarrow {}^7F_2$). The decays are well described by a single exponential function for all Eu^{3+} concentrations in the different crystalline phases. As an example, Fig. 10 shows the decays for the samples 1D (Eu^{3+} 1 %-δ), 1A (Eu^{3+} 1 %-α), and 1DA (Eu^{3+} 1 %-δ + α). As can be seen in Table 4, the lifetime values are shorter in the case of the delta phase, which agrees well with the lower site symmetry for the Eu^{3+} ions in this phase and the more electric-dipole character shown by the $^5D_0 \rightarrow {}^7F_2$ transition. The lifetimes of the α and (δ + α) phases are similar, which agrees with the results found in the TRFLN spectra.

As a final comment, we would like to stress the *finesse* of TRFLN spectroscopy to detect small local crystal field variations. In our case, despite the small energy difference between the positions of the $^5D_0$ singlet level in both δ and α phases (0.0004 eV), it is possible not only to clearly discern the different symmetries of the main site that the rare earth occupies in the crystalline matrix but also to determine what kind of contributions in rare earth emission come from site distribution peripherals occupied by the chromophore. In the latter case, although these contributions may be small, the spectral information can be decisive when it comes to applications related to the functionalization of the nanoparticle surface. On the other hand, the top-notch optical performance of the δ-KY_3F_{10}:Eu^{3+} materials and the high chemical and thermal stability (from cryogenic up to 400 °C) make them of high interest in several photonic fields. Coupling/functionalizing these compounds with other lanthanides opens up a vast spectrum for their application in sensing and nanothermometry (for example by using the pair Eu^{3+}/Tb^{3+}), or in solid-state lighting devices (combining the yellow-orangish emission of the samples with blue InGaN chips to fabricate w-LEDs).

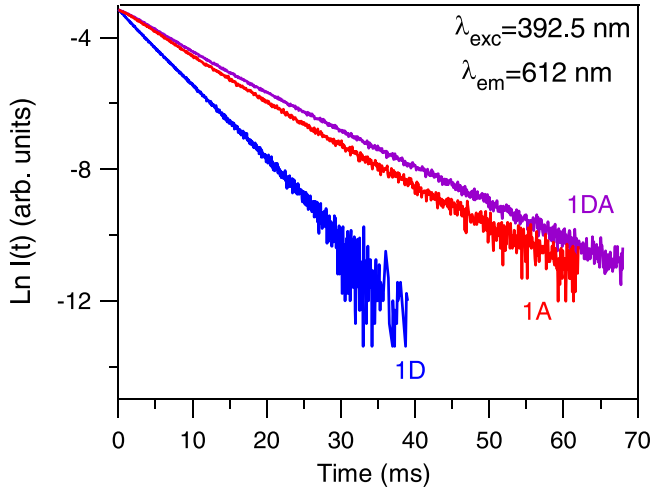

Fig. 10. Semilogarithmic plot of the fluorescence decays of the $^5D_0$ level obtained under excitation at 392.5 nm and collecting the luminescence at 612 nm for the samples 1D (Eu^{3+} 1 %-δ), 1 A (Eu^{3+} 1 %-α), and 1DA (Eu^{3+} 1 %-δ + α).

Table 4
Lifetimes of the $^5D_0$ level obtained by exciting at 392.5 nm in the $^7F_0 \rightarrow {}^5L_6$ transition and collecting the luminescence at 612 nm. The coefficient of determination R^2 is also included.

% Eu^{3+}	Lifetime (ms)					
	δ	R^2	α	R^2	δ + α	R^2
1	4.28	0.9993	7.01	0.9996	7.79	0.9995
3	4.00	0.9997	6.16	0.9998	7.23	0.9993
5	3.69	0.9996	5.08	0.9992	6.20	0.9994

4. Conclusions

The crystallographic nature and spectroscopic features concerning the site-selective symmetries in Eu^{3+}-doped KY_3F_{10} compounds with α and δ crystal phases have been investigated in detail by TRFLN spectroscopy. For that purpose, samples containing different amounts of the luminescent Eu^{3+} ion (1, 3, 5 mol%) were synthesized yielding powders with single δ-phase, single α-phase, and a mixture of both phases. The results obtained lead to the following main conclusions:

- A new, fast, and easy coprecipitation method is developed to prepare the δ-phase compounds yielding spherical particles. This strategy represents a remarkable improvement in comparison to the existing synthesis for this structure.
- The XRD results are well corroborated with the morphological, FT-IR, DLS, and TG/DSC analyses. Samples containing the mixture (δ + α) exhibited a behavior very close to that of samples with the α-phase, thus suggesting the predominance of this phase in the mixture, which is supported by the estimated phase fractions obtained from the Rietveld refinement.
- TRFLN experiments confirm the existence of Eu^{3+} ions in the expected crystallographic symmetries (C_{2v} in δ, and C_{4v} in α). The laser tuning facility of this technique has made it possible to discriminate the presence of europium ions lying at low-symmetry sites near the surface of the crystalline nanoparticles, with an optical response similar to that produced in glasses.
- The lifetime values agree well with the different site symmetries for the Eu^{3+} ions and the electric-dipole character of the $^5D_0 \rightarrow {}^7F_2$ transition.
- From an energetic point of view, the emission efficiency of the δ phase is much higher (> 20 times) than the α one for all the spectral components in the TRFLN measurements, which is a point worthy of praise.

As per the above points, the results underscore the huge potential of the unknown δ-phase and the importance of using very precise spectroscopic techniques, as is the case of TRFLN, to shed light on the comprehension of the optical response of the luminescent dopants, which is a matter of concern when developing photonic materials for top-notch applications.

Author statement

All authors contributed equally to perform the required experiments, analyze the data and write the paper. All authors reviewed and edited the manuscript.

Data Availability

Data will be made available on request.

Declaration of Competing Interest

The authors declare that they have no known competing financial interests or personal relationships that could have appeared to influence the work reported in this paper.

Acknowledgments

This work was supported financially by the Spanish MCIN (Grant PID2020-116149GB-I00 and PID2020-115419GB/C-22 funded by MCIN/AEI/10.13039/501100011033) and the University of the Basque Country (GIU21/006). P. Serna also thanks the Spanish MCIN for an FPU predoctoral contract (FPU18/04511 funded by MCIN/AEI /10.13039/501100011033 and by "ESF Investing in your future").

Appendix A. Supporting information

Supplementary data associated with this article can be found in the online version at doi:10.1016/j.jallcom.2023.170020.

References

[1] J. Wu, J. Wang, J. Lin, Y. Xiao, G. Yue, M. Huang, Z. Lan, Y. Huang, L. Fan, S. Yin, T. Sato, Dual functions of YF_3:Eu^{3+} for improving photovoltaic performance of dye-sensitized solar cells, Sci. Rep. 3 (2013) 1–5, https://doi.org/10.1038/srep02058

[2] B.M. Tissue, Synthesis and luminescence of lanthanide ions in nanoscale insulating hosts, Chem. Mater. 10 (1998) 2837–2845, https://doi.org/10.1021/cm9802245

[3] T. Grzyb, M. Węcławiak, T. Pędziński, S. Lis, Synthesis, spectroscopic and structural studies on YOF, LaOF and GdOF nanocrystals doped with Eu^{3+}, synthesized via stearic acid method, Opt. Mater. 35 (2013) 2226–2233, https://doi.org/10.1016/j.optmat.2013.06.007

[4] A. Podhorodecki, A. Noculak, M. Banski, B. Sojka, A. Zelazo, J. Misiewicz, J. Cichos, M. Karbowiak, B. Zasonska, D. Horak, B. Sikora, D. Elbaum, T. Dumych, R. Bilyy, M. Szewczyk, Lanthanides fluorides doped nanocrystals for biomedical applications, ECS Trans. 61 (2014) 115–125, https://doi.org/10.1149/06105.0115ecst

[5] A. Jain, P.G.J. Fournier, V. Mendoza-Lavaniegos, P. Sengar, F.M. Guerra-Olvera, E. Iñiguez, T.G. Kretzschmar, G.A. Hirata, P. Juárez, Functionalized rare earth-doped nanoparticles for breast cancer nanodiagnostic using fluorescence and CT imaging, J. Nanobiotechnol. 16 (2018) 1–18, https://doi.org/10.1186/s12951-018-0359-9

[6] J. Periša, J. Papan, S.D. Dolić, D.J. Jovanović, M.D. Dramićanin, Multicolor-tunable emissions of YOF: Ln^{3+}/Yb^{3+} (Ln^{3+} = Ho^{3+}, Er^{3+}, Tm^{3+}) nanophosphors, Dye. Pigment. 155 (2018) 233–240, https://doi.org/10.1016/j.dyepig.2018.03.047

[7] C. Sassoye, G. Patriarche, M. Mortier, High yield syntheses of reactive fluoride $K_{1-x}(Y,Ln)_xF_{1+2x}$ nanoparticles, Opt. Mater. 31 (2009) 1177–1183, https://doi.org/10.1016/j.optmat.2008.12.013

[8] F. Auzel, Upconversion and Anti-Stokes Processes with *f* and *d* Ions in Solids, Chem. Rev. 104 (2004) 139–173.

[9] L. Zhu, J. Meng, X. Cao, Sonochemical synthesis of monodispersed KY_3F_{10}:Eu^{3+} nanospheres with bimodal size distribution, Mater. Lett. 62 (2008) 3007–3009, https://doi.org/10.1016/j.matlet.2008.01.096

[10] C. Cao, Hydrothermal synthesis, phase evolution, and optical properties of Eu^{3+}-doped KF-YF_3 system materials, J. Mater. Res. Soc. 27 (2012) 2988–2995, https://doi.org/10.1557/jmr.2012.331

[11] S. Goderski, M. Runowski, S. Lis, Synthesis of luminescent KY_3F_{10} nanopowder multi-doped with lanthanide ions by a co-precipitation method, J. Rare Earths 34 (2016) 808–813, https://doi.org/10.1016/S1002-0721(16)60098-4

[12] M. Runowski, Color-tunable up-conversion emission of luminescent-plasmonic, core/shell nanomaterials - KY_3F_{10}:Yb^{3+},Tm^{3+}/SiO_2-NH_2/Au, J. Lumin. 186 (2017) 199–204, https://doi.org/10.1016/j.jlumin.2017.02.032

[13] M. Chen, P. Loiko, J.M. Serres, S. Veronesi, M. Tonelli, M. Aguiló, F. Díaz, S.Y. Choi, J.E. Bae, F. Rotermund, S. Dai, Z. Chen, U. Griebner, V. Petrov, X. Mateos, Fluorite-type Tm^{3+}:KY_3F_{10}: a promising crystal for watt-level lasers at ~1.9 μm, J. Alloy. Compd. 813 (2020) 152176, , https://doi.org/10.1016/j.jallcom.2019.152176

[14] F. Le Berre, E. Boucher, M. Allain, G. Courbion, Synthesis, stability and zeolitic behavior of δ-ALn_3F_{10},xH_2O and γ-$ThLn_2F_{10}$,H_2O phases (Ln=lanthanide), J. Mater. Chem. 10 (2000) 2578–2586, https://doi.org/10.1039/b002520h

[15] P. Serna-Gallén, H. Beltrán-Mir, E. Cordoncillo, The unexplored δ-phase of KY_3F10: toward novel Eu^{3+}-doped nanoplates with a 'super-diamond' structure for optical applications, J. Mater. Res. Technol. 15 (2021) 6940–6946, https://doi.org/10.1016/j.jmrt.2021.11.060

[16] P. Serna-Gallén, H. Beltrán-Mir, E. Cordoncillo, The pH-dependent reactions in the sonochemical synthesis of luminescent fluorides: the quest for the formation of KY_3F_{10} crystal phases, Ultrason. Sonochem. 87 (2022) 106059, , https://doi.org/10.1016/j.ultsonch.2022.106059

[17] P. Villars and K. Cenzual, Eds., KY_3F_{10} Crystal Structure: Datasheet from 'PAULING FILE Multinaries Edition – 2012' in SpringerMaterials ⟨https://materials.springer.com/isp/crystallographic/docs/sd_0552093⟩.

[18] P. Villars and K. Cenzual, Eds., δ-KY_3F_{10}·xH_2O (KY_3F_{10}[H_2O]) Crystal Structure: Datasheet from 'PAULING FILE Multinaries Edition – 2012′ in SpringerMaterials ⟨https://materials.springer.com/isp/crystallographic/docs/sd_1004004⟩.

[19] K. Momma, F. Izumi, VESTA 3 for three-dimensional visualization of crystal, volumetric and morphology data, J. Appl. Crystallogr 44 (2011) 1272–1276, https://doi.org/10.1107/S0021889811038970

[20] P.P. Fedorov, M.N. Mayakova, S.V. Kuznetsov, V.V. Voronov, R.P. Ermakov, K.S. Samarina, A.I. Popov, V.V. Osiko, Co-precipitation of yttrium and barium fluorides from aqueous solutions, Mater. Res. Bull. 47 (2012) 1794–1799, https://doi.org/10.1016/j.materresbull.2012.03.027

[21] B.E.G. Lucier, K.E. Johnston, D.C. Arnold, J.L. Lemyre, A. Beaupré, M. Blanchette, A.M. Ritcey, R.W. Schurko, Comprehensive solid-state characterization of rare earth fluoride nanoparticles, J. Phys. Chem. C 118 (2014) 1213–1228, https://doi.org/10.1021/jp408148b

[22] C. Caron, D. Boudreau, A.M. Ritcey, Luminescent properties of europium-doped (H_3O)Y_3F_{10}·xH_2O nanocrystals, J. Mater. Chem. C 3 (2015) 9955–9963, https://doi.org/10.1039/c5tc02527c

[23] B. Richard, J.L. Lemyre, A.M. Ritcey, Nanoparticle size control in microemulsion synthesis, Langmuir 33 (2017) 4748–4757, https://doi.org/10.1021/acs.langmuir.7b00773

[24] O.V. Andrrev, I.A. Razumkova, A.N. Boiko, Synthesis and thermal stability of rare earth compounds REF_3, REF_3·nH_2O and (H_3O)RE_3F_{10}·nH_2O (RE = Tb – Lu, Y), obtained from sulphide precursors, J. Fluor. Chem. 207 (2018) 77–83, https://doi.org/10.1016/j.jfluchem.2017.12.001

[25] D. Das, S.K. Gupta, K. Sudarshan, Europium luminescence as a structural probe to understand defect evolution in CeO_2/Eu^{3+}, M^{3+} (M = Y and La): contrasting role of codopant ionic size, J. Mater. Sci. 56 (2021) 17205–17220, https://doi.org/10.1007/s10853-021-06366-3

[26] T.N.L. Tran, A. Chiasera, A. Lukowiak, M. Ferrari, Eu^{3+} as a powerful structural and spectroscopic tool for glass photonics, Materials 15 (2022) 1–11, https://doi.org/10.3390/ma15051847

[27] F. Ariese, A.N. Bader, C. Gooijer, Fluorescence line-narrowing spectroscopy for probing purposes in bioanalytical and environmental chemistry, TrAC - Trends Anal. Chem. 27 (2008) 127–138, https://doi.org/10.1016/j.trac.2008.01.002

[28] A. Szabo, Laser-induced fluorescence-line narrowing in ruby, Phys. Rev. Lett. 25 (1970) 924–926, https://doi.org/10.1103/PhysRevLett.25.924

[29] M. Reppert, V. Naibo, R. Jankowiak, Accurate modeling of fluorescence line narrowing difference spectra: Direct measurement of the single-site fluorescence spectrum, J. Chem. Phys. 133 (2010) 014506, , https://doi.org/10.1063/1.3455890

[30] T. Vo-Dinh, N.H. Velthorst, D.S. Moore, B. Schrader, Nomenclature, symbols, units, and their usage in spectrochemical analysis XVI. Laser-based molecular spectrometry for chemical analysis - Luminescence (IUPAC Recommendations 1997), Pure Appl. Chem. 69 (1997) 1435–1449.

[31] L.A. Riseberg, Physical review letters 27, Phys. Rev. Lett. 28 (1972) 786–789.

[32] J.A. Capobianco, P. Proulx, B. Andrianasolo, B. Champagnon, Nucleation kinetic studies of a europium-doped aluminosilicate glass: low-frequency inelastic scattering and fluorescence line narrowing, Phys. Rev. B - Condens. Matter Mater. Phys. 43 (1991) 10031–10035, https://doi.org/10.1126/science.267.5198.713

[33] J. Fidy, M. Laberge, A.D. Kaposi, J.M. Vanderkooi, Fluorescence line narrowing applied to the study of proteins, Biochim. Biophys. Acta - Protein Struct. Mol. Enzymol. 1386 (1998) 331–351, https://doi.org/10.1016/S0167-4838(98)00101-0

[34] L.A. Riseberg, Laser-induced fluorescence-line-narrowing spectroscopy of glass:Nd, Phys. Rev. A 7 (1973) 671–678.

[35] V.P. Tuyen, T. Hayakawa, M. Nogami, J.R. Duclre, P. Thomas, Fluorescence line narrowing spectroscopy of Eu^{3+} in zinc-thallium-tellurite glass, J. Solid State Chem. 183 (2010) 2714–2719, https://doi.org/10.1016/j.jssc.2010.08.025

[36] Y. Huang, H.J. Seo, Multisite structure of PbWO4:Eu^{3+} crystals investigated by site-selective laser-excitation spectroscopy, J. Phys. Chem. A 113 (2009) 5317–5323, https://doi.org/10.1021/jp901099h

[37] Y. Huang, L. Shi, E.S. Kim, H.J. Seo, Site-selective spectroscopy and crystallographic sites of Eu^{3+} ions doped in Gd_2BaZnO_5, J. Appl. Phys. 105 (2009) 013512, , https://doi.org/10.1063/1.3056167

[38] P. Serna-Gallén, H. Beltrán-Mir, E. Cordoncillo, Tuning the optical and photoluminescence properties of high efficient Eu^{3+}-doped KY_3F_{10} phosphors by different synthetic approaches, Opt. Laser Technol. 136 (2021) 106734, , https://doi.org/10.1016/j.optlastec.2020.106734

[39] I.S. Osad'ko, Selective spectroscopy of chromophore doped polymers and glasses, Adv. Polym. Sci. Springer, Berlin, Heidelberg, 1994, pp. 122–186, https://doi.org/10.1007/bfb0008695

[40] I.I. Abram, R.A. Auerbach, R.R. Birge, B.E. Kohler, J.M. Stevenson, Narrow-line fluorescence spectra of perylene as a function of excitation wavelength, J. Chem. Phys. 63 (1975) 2473–2478, https://doi.org/10.1063/1.431688
[41] P.A. Tanner, Some misconceptions concerning the electronic spectra of tri-positive europium and cerium, Chem. Soc. Rev. 42 (2013) 5090–5101, https://doi.org/10.1039/c3cs60033e
[42] K. Binnemans, Interpretation of europium(III) spectra, Coord. Chem. Rev. 295 (2015) 1–45, https://doi.org/10.1016/j.ccr.2015.02.015
[43] R. Balda, J. Fernández, J. Adam, Time-resolved fluorescence-line narrowing and energy-transfer studies in a doped fluorophosphate glass, Phys. Rev. B - Condens. Matter Mater. Phys. 54 (1996) 12076–12086, https://doi.org/10.1103/PhysRevB.54.12076